High-energy ball-milling constructing P-doped g-C₃N₄/MoP heterojunction with Mo—N bond bridged interface and Schottky barrier for enhanced photocatalytic H₂ evolution

Xuehua Wang [a], Xianghu Wang [b], Wenli Tian [b], Alan Meng [b,*], Zhenjiang Li [a,c,**], Shaoxiang Li [c], Lei Wang [b], Guicun Li [a]

[a] College of Materials Science and Engineering, Qingdao University of Science and Technology, Qingdao 266042, Shandong, PR China
[b] Key Laboratory of Optic-electric Sensing and Analytical Chemistry for Life Science, MOE. College of Chemistry and Molecular Engineering, Qingdao University of Science and Technology, Qingdao 266042, Shandong, PR China
[c] Shandong Engineering Technology Research Center for Advanced Coating, Qingdao University of Science and Technology, Qingdao 266042, PR China

ARTICLE INFO

ABSTRACT

The critical prerequisite for realizing the industrial application of photocatalytic technology lies on developing efficient photocatalyst through reasonable and large-scale modification strategy. Herein, the rapid and solvent-free high-energy ball-milling procedure was adopted to modify graphitic carbon nitride (g-C₃N₄) on a large-scale by phosphorus (P) atom doping and molybdenum phosphide (MoP) decorating. It is confirmed that P doping can introduce a mid-gap state in the band gap of g-C₃N₄, broadening the light responsive region and enhancing the electrical conductivity of g-C₃N₄. The Mo—N bond at the interface of P-doped g-C₃N₄ and MoP acting as electrons "delivery channels" facilitates the charge transfer from P-doped g-C₃N₄ to MoP, while the Schottky barrier promotes the separation of photocarriers. As a result, the optimized P-doped g-C₃N₄/MoP photocatalyst performs an improved H₂ evolution rate of 4917.83 μmol·g⁻¹·h⁻¹ and a favorable H₂ production stability. This work offers a replicable prototype on adopting high-energy ball-milling to modify photocatalyst.

1. Introduction

The rapid development of industrial society brings about severe energy and environmental pressures, which urge the appearance of the new-style and sustainable energy utilization and conversion pattern. The capture and conversion of solar energy via water photolysis affords a promising way to convert inexhaustible solar energy to hydrogen (H₂) energy, realizing a green and benign energy circulation due to that the combustion product of H₂ is still water [1–4]. Benefits to the above reasons, photocatalytic H₂ production have long been recognized, and attracted the intense attention from researchers around the world. Hitherto, researchers have thrown tremendous effort on exploring efficient photocatalytic materials. Compared to the widely studied metal-containing photocatalysts, metal-free photocatalysts (such as g-C₃N₄, BP, h-BN, etc.) with plentiful and cheap raw materials, high stability and harmless to the environment and human, are getting more and more attention recently [5–7]. Graphitic carbon nitride (g-C₃N₄) is

an organic polymeric semiconductor with 2D layer crystal configuration, which has been widely used as H₂ evolution photocatalyst, due to its suitable band gap (2.7 eV) and conduction band potential (−0.95 eV), low-cost composition elements (C and N), easily preparation technology and exceptional thermal and chemical stability [8–10]. However, the confined visible-light absorption, inferior photocarrier mobility and separation give rise to the very low H₂ production rate of g-C₃N₄. Therefore, the exploration on modifying g-C₃N₄ to maximize its photocatalytic performance has become a sustained research hotspot in recent years.

Various strategies have been applied to provoke the photocatalytic property of g-C₃N₄, such as, elements doping, cocatalyst modifying and heterojunction constructing [11,12]. Therein, introducing heteroatoms into g-C₃N₄ skeleton is considered as an effective means to tune the optical/electronic properties by inserting new impurity levels in the band gap of g-C₃N₄ [9]. Among various dopants (such as, O, S, B, I, etc.), P is reported to be an ideal dopant of g-C₃N₄, because the lone electrons

in P atom could induce the delocalization effect in p-conjugated triazine ring of g-C₃N₄, thus introducing electron-rich centers around P-doped sites [13,14]. For example, Qiao et al. synthesized a P-doped g-C₃N₄ photocatalyst through calcining at 500 °C in N₂ flow for 3 h to realize P doping followed by calcining at 500 °C in air for 2 h to conduct out thermal exfoliation, in which, the DFT calculation and experimental studies confirmed that P doping can effectively extend the light-responsive region of g-C₃N₄ [15]. Jia et al. doped P into g-C₃N₄ through calcination method (550 °C for 4 h) using phosphoric acid and cyanuric acid-melamine complex as the phosphorus source and the supramolecular precursor, respectively. It is verified that P atom doping intensifies the visible-light utilization capacity and the photocatalytic activity of g-C₃N₄ [16]. In addition to P doping, constructing heterojunction photocatalyst is also an effective strategy to enhance the photocatalytic activity of g-C₃N₄. Schottky heterojunction is a type of junction resulting from the intimate contact of a metal or semimetal with a semiconductor [17], which can accelerate photocatalytic reaction dynamics through promoting photocarriers separation, thus can significantly improve the H₂ production activity. For example, Xu et al. synthesized a NiS/g-C₃N₄ Schottky junction via solvothermal method at 120 °C for 20 h, which achieves a photocatalytic H₂ evolution activity from "zero" to "one" [18]. Li et al. fabricated a 2D–2D CoP/g-C₃N₄ Schottky junction through a solvothermal followed by phosphorization process. The synthesized photocatalyst exhibits a higher H₂ evolution rate than that of Pt/g-C₃N₄ [19]. As known from the above literatures, the fabrication of Schottky junction can obviously improve the photocatalytic activity, due to that the Schottky barrier can inhibit the reflux of photogenerated electrons from metal (or semimetal) to semiconductor, and enhance the separation efficiency of photocarriers. Nevertheless, it is undeniable that the mobility of photogenerated electrons in Schottky junction will be restrained to some extent, due to that the transfer of photogenerated electrons from semiconductor to metal (or semimetal) should require to overcome the energy barrier of Schottky barrier. Therefore, ensuring photoexcited carriers separation while promoting its efficient transfer is an important guarantee for realizing high-efficiency photocatalytic performance. As known, the intimate interface contact with interfacial chemical bond would provide rapid charge transfer channels to further accelerate the transfer process of photogenerated carriers [20]. Inspired by this point, the H₂ evolution activity of Schottky junction photocatalyst could be further enhanced by synergistically establishing Schottky barrier for enhancing separation efficiency and interfacial chemical bond connection for accelerating transfer rate of photogenerated electrons.

In electrocatalytic HER field, Molybdenum phosphide (MoP) has been considered a promising substitute to Pt, due to its favorable electrical conductivity, superior chemical stability and Pt-like electronic structure [21]. In addition, according to the reported literatures, MoP possesses the metallic characteristic with large work function and intense light absorbance capacity [22,23]. Therefore, it is imaginable that when MoP was combined with P-doped g-C₃N₄ by forming interfacial chemical bond, the Schottky barrier at the interface of P-doped g-C₃N₄ and MoP would accelerate the photocarriers separation process, while the interfacial chemical bond would serve as the charge transfer channel for promoting the transfer efficiency of photocarriers in P-doped g-C₃N₄/MoP heterojunction, thus the photocatalytic performance of g-C₃N₄ can be effectively improved. In another aspect, the reported strategies to realize P doping or Schottky junction construction are usually the calcination or solvent-required chemical methods, which are high energy consumption and environmentally hazardous, especially, the low-throughput greatly limits their practical application. Therefore, developing an advanced preparation technology meeting the requirements of sustainable development and large-scale application is the most urgent and challenging task.

Very recently, high-energy ball-milling induced mechanochemical reaction has stimulated increasing attention in composite material preparation due to its simple, rapid, easily scaled-up and economical

traits. During high-energy ball-milling process, the mechanical efficiency including impact, shear and compression between milling ball and materials can effectively decrease the grain size and expose more active edges and surfaces, improving the reactivity of material. Besides, a part of mechanical energy would be converted to thermal energy, raising the local temperature of the material. All of the above effects would contribute to the chemical reaction between the grinding materials by promoting the breakdown and recombination of the chemical bonds [8,24]. Therefore, it is expectable that through high-energy ball-milling technology, not only that the heteroatom P can be doped in g-C₃N₄, but also the intimate interfacial combination can be constructed between the P-doped g-C₃N₄ and MoP. Nevertheless, there have been no reports regarding this until now.

In this work, a novel and efficient H₂ evolution photocatalyst P-doped g-C₃N₄/ MoP was successfully synthesized via a simple, rapid, solvent-free and large-scale high-energy ball-milling process. Under the intense mechanical action of high-energy ball-milling, P atoms in NaH₂PO₂·2H₂O were doped into g-C₃N₄ and MoP nanoparticles were intimately embedded on the surface of P-doped g-C₃N₄ through Mo—N bond (the detailed preparation process was illustrated in Fig. 1). Systematic characterization and density functional theory (DFT) calculation confirmed that under the synergistic effect of P doping, Mo—N bond connecting and Schottky barrier, P-doped g-C₃N₄/MoP exhibits increased light absorbance capacity, the smaller interface charge transfer resistance, the inhibited photocarriers recombination and the accelerated H₂ evolution reaction dynamics, thereby leading to the excellent photocatalytic H₂ production rate in the absence of any noble-metal cocatalyst. This work provides an efficient photocatalyst modified by element doping, interfacial chemical bonding and Schottky barrier, and offers an inspiration on preparing photocatalyst through versatile and mass producible high-energy ball-milling method.

2. Experimental section

2.1. Materials

Urea, Sodium hypophosphite (NaH₂PO₂·2H₂O), triethanolamine (TEOA), and ethanol were purchased from Sinopharm Chemical Reagent Co., Ltd. Sodium molybdate dihydrate (Na₂MoO₄·2H₂O) was purchased from Tianjin Fengchuan Chemical Reagent Technology Co., LTD. The above analytical grade chemical reagents were used directly without further purification.

2.2. Preparation of photocatalysts

2.2.1. Preparation of g-C₃N₄

The synthesis of g-C₃N₄ was synthesized based on our previous research.[8] Typically, 10 g urea was encapsulated in a covered alumina crucible, which was then calcined at 550 C with a heating rate of 5 °C/min for 4 h in muffle furnace. The obtained light-yellow fine powder was denoted as CN.

2.2.2. Preparation of P-doped g-C₃N₄ (PCN)

The P-doped g-C₃N₄ was prepared by high-energy ball-milling method. In a typical process, 1 g of the as-abstained g-C₃N₄ and a certain amount of NaH₂PO₂·2H₂O were mixed and sealed in a 50 mL zirconium oxide grinding jar with 8 zirconium oxide milling balls (diameter: ~10 mm). The P doping process was conducted out on high-energy ball-milling machine (Retsch, Emax) equipped with circulating cooling water system at 1000 rpm for 1 h. The final mPCN ("m" represents the mass ratio of NaH₂PO₂·2H₂O to g-C₃N₄, m =0, 0.3, 0.5, 0.7, 0.9, 1.2 and 1.5) was obtained by washing with deionized water for several times, and drying at 60 °C for 5 h in vacuum oven, where.

2.2.3. Preparation of MoP

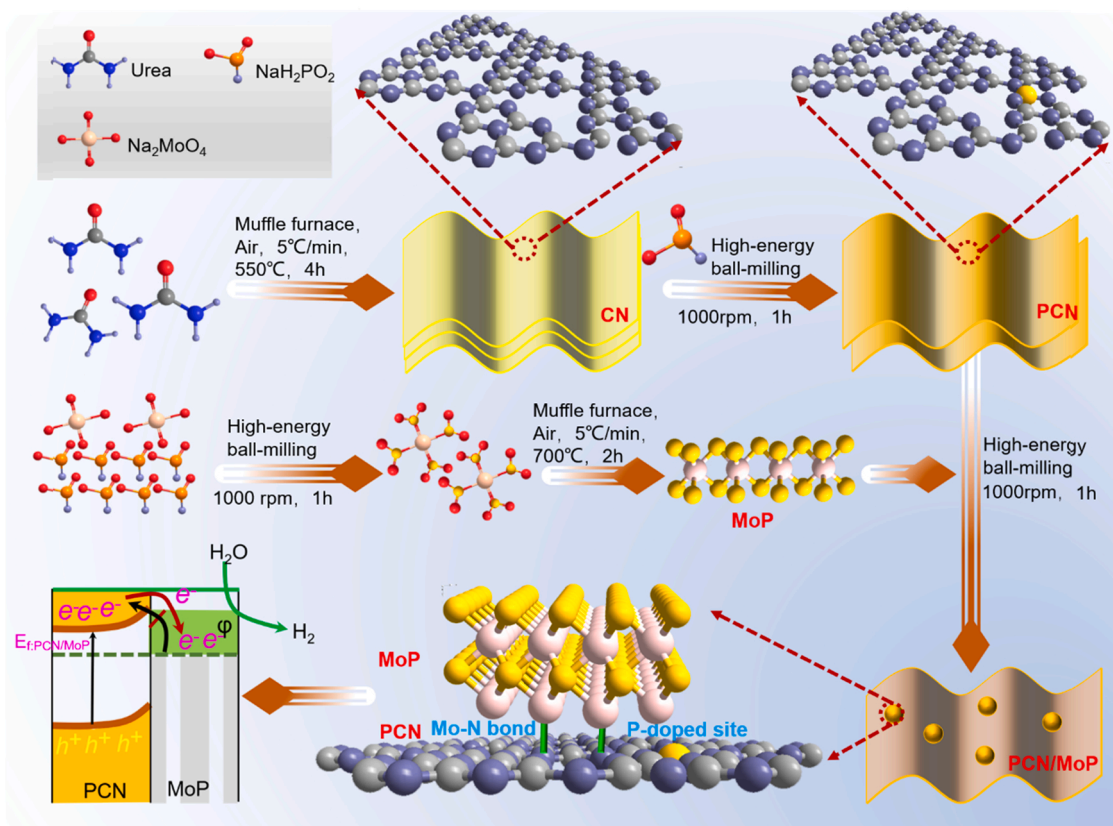MoP was synthesized through a ball-milling coupled by calcination

Fig. 1. Schematic presentation of the synthetic route of PCN/MoP heterojunction.

method. Specifically, 1 g Na$_2$MoO$_4$·2H$_2$O and 10 g NaH$_2$PO$_2$·H$_2$O were sealed in 50 mL zirconium oxide grinding jar with 8 zirconium oxide milling balls (diameter: ~10 mm) and milled at 1000 rpm for 1 h. The obtained precursor was collected and transferred into a covered alumina crucible, then it was calcined at 700 °C with a heating rate of 5 °C/min for 2 h in muffle furnace. The obtained powder was filtrated under reduced pressure, washed with deionized water and ethanol for several times, and dried at 60 °C for 5 h in vacuum oven.

2.2.4. Preparation of P-doped g-C$_3$N$_4$/MoP (PCN/MoP)

PCN/MoP heterojunction photocatalyst were prepared through high-energy ball-milling procedure. In detail, 1 g the PCN with different P doping content and MoP were grinded at 1000 rpm for 1 h in high-energy ball-milling machine (Retsch, Emax). To investigate the effect of MoP content on the photocatalytic H$_2$ evolution activity, various PCN/nMoP ("n" represents the mass ratio of MoP to PCN, n = 0.01, 0.03, 0.05, 0.07 and 0.09) were synthesized, where the mass ratio of NaH$_2$PO$_2$·H$_2$O to CN was fixed at 0.9:1. In the following description, the PCN/MoP represents the PCN/MoP sample with the mass ratio of 0.9:1 and 0.05:1 for NaH$_2$PO$_2$·H$_2$O to CN and MoP to PCN, respectively. For comparison, CN/MoP was synthesized by milling the pristine CN with MoP, and the mass ratio of MoP to CN was 0.05:1.

2.3. Characterization

The morphology and microstructure were observed using JEM-F200 Field emission transmission electron microscope (TEM) equipped with energy dispersive X-ray spectrometer. The crystalline phase information was obtained through Bruker D8 Advance X-ray diffraction (XRD) at 40 kV voltage and 40 mA current under Cu Kα irradiation (0.15406 nm). The surface elements and chemical state were characterized on Thermo fisher Escalab 250Xi X-ray photoelectron spectroscopy (XPS) with monochromatic Al Kα radiation, and the XPS data was calibrated by C 1s

spectrum (binding energy at 284.8 eV). The molecular structure information was conducted on LabRAM HR Evolution Raman spectrometer with 325 nm excitation wavelength. The light absorption capacity was analyzed on PerkinElmer Lambda 750 S UV–vis spectrophotometer with BaSO$_4$ as the standard reference material. The photocarriers separation efficiency was characterized by F-4600 spectrofluorometer (375 nm excitation wavelength) and Edinburgh FLS 980 transient fluorescence spectrometer (375 nm excitation wavelength). The defect state was characterized by JEOL JES-FA200 paramagnetic resonance (EPR) spectrometer with microwave frequency of 9065.41 MHz, modulation amplitude of 2 G, modulation frequency of 100 kHz and microwave power of 0.998 mW at 298 K in air atmosphere. The secondary cutoff binding energy was measured by AXIS SUPRA X-ray photoelectron spectroscopy with He I as the excitation source. All the photo-electrochemical and electrochemical measurements were conducted by standard three-electrode system on CHI-660E electrochemical work-station with Pt slice, Ag/AgCl and FTO collector coating photocatalyst as reference electrode, counter electrode and working electrode, respectively. The 0.5 M Na$_2$SO$_4$ aqueous solution was adopted as electrolyte.

2.4. Photocatalytic activity measurements

The photocatalytic hydrogen evolution experiments were performed in a top-irradiation Pyrex reaction vessel (250 mL) connected with all glass automatic on-line trace gas analysis system (Labsolar-6A, Beijing PerfectLight). In detail, 10 mg of photocatalyst was dispersed into 100 mL water solution containing 20 mL TEOA sacrificial agent. Before reaction, the solution was evacuated thoroughly to remove the solved air in the reaction system. 300 W Xenon-lamp (PLS-SXE300D, Beijing Perfectlight) was adopted as the light source, and the temperature of the solution was kept as 5 °C through circulating cooling water system (Low-constanttemp, Beijing Perfectlight). The evolved gas was analysized automatically by GC 7900 gas chromatograph with Ar carrier gas

and TCD detector (Techcomp).

2.5. Theoretical calculations

Periodic plane-wave density functional theory (DFT) calculations were performed using the Vienna ab initio simulation package (VASP) [25,26]. The exchange-correlation was described by the Perdew-Burke-Ernzerhof revised for solids (PBE) method of the generalized gradient approximation (GGA) with a plane-wave kinetic cutoff energy of 500 eV [27]. The projector augmented wave (PAW) depicted non-spherical contributions to the core from the gradient corrections [28–30]. The long-range interaction was characterized by the DFT-D3 method of Grimme with zero dampings [31]. The unit cell and force optimized convergence threshold of internal forces and electronic relaxation was set to 10^{-5} eV. A 3 * 3 * 1 Monkhorst-pack grid sampled the Brillouin zone with a smearing broadening of 0.02 eV. The band structure calculation and data post-processing are performed by vaspkit [32].

3. Results and discussion

3.1. Photocatalyst preparation

The PCN/MoP photocatalytic was fabricated following the procedure in Fig. 1. In detail, under the intense mechanical action of high-energy ball-milling including collision, extrusion and shear, the instantaneous temperature on the surface of solids was enhanced, resulting in the increased reaction activity between $NaH_2PO_2 \cdot 2H_2O$ and $g\text{-}C_3N_4$, and embowing P atoms enter $g\text{-}C_3N_4$ by replacing C atoms. In addition, the high-speed collision between grinding ball and materials (PCN and MoP) and the increased local high temperature pulses motivated the chemical bond breaking and reorganizing reaction, thus giving rise to the intimate interfacial chemical bond (Mo-N) bonded heterointerface between PCN and MoP.

3.2. Materials characterizations

The crystalline phase information of the as-prepared photocatalysts were investigated by X-ray diffraction (XRD). As shown in Fig. 2a, the original CN exhibits two distinct diffraction peaks at 13.4° and 27.7°, corresponding to the (100) and (002) plane of graphitic carbon nitride
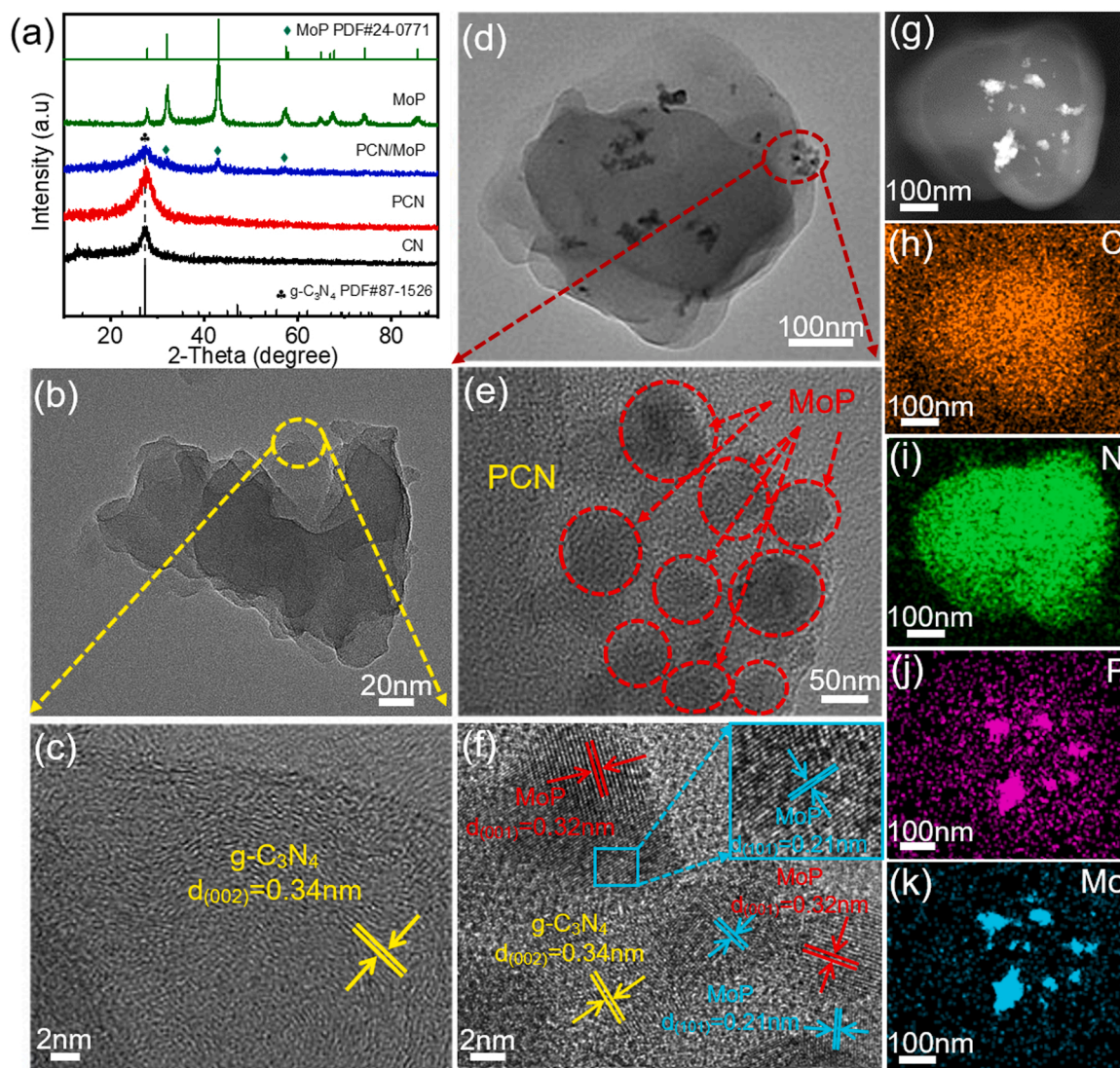

Fig. 2. (a) XRD patterns of CN, PCN, PCN/MoP and MoP. (b, c) TEM and HRTEM of PCN. (d-f) TEM and HRTEM of PCN/MoP. (g-k) TEM image and the corresponding element mapping of PCN/MoP.

(JCPDS 87–1526). The XRD pattern of PCN is almost consistent with the pristine CN, demonstrating that P atom doping cannot destroy the crystalline structure of CN. In addition, it can be observed that the (100) plane in PCN vanished, and the peak of (002) plane in PCN gets more intense compared with that in the pristine CN, which should be contributed to that the high-energy ball-milling process not only introduce P atom into g-C_3N_4, but also bring about crystal orientation, endowing more (002) plane with abundant low-coordinated atoms expose to provide more high-active sites [8,33]. For the XRD pattern of MoP, the cuspidal peaks at 27.94°, 32.17°, 43.1°, 57.47°, 64.93°, 67.85° and 74.33° can be assigned to the (001), (100), (101), (110), (111), (102) and (201) planes of hexagonal MoP (JCPDS 65–6487), suggesting the successful preparation of MoP with high crystallinity. In the XRD pattern of PCN/MoP, both the diffraction peaks of g-C_3N_4 and MoP can be discovered, confirms the successful preparation of PCN/MoP heterojunction photocatalyst. It can be also noted that the (002) plane peak of PCN in PCN/MoP presents decrease than that of PCN, which should be explained to that MoP was depositing on the surface of PCN.

To further characterize the morphology and microstructure of the synthesized photocatalyst, TEM, HRTEM and element mapping were carried out. Fig. S1a is the TEM image of pristine CN. It can be discovered that the original CN exhibits the large and curly sheet morphology. In comparison, as observed in Fig. S1b and Fig. 2b, PCN presents the flat and smaller nanosheet structure, more importantly, it can be noted that the dispersity of PCN nanosheet is higher than that of CN, which should be ascribed to the strong crushing effect during high-energy ball-milling process, and would be beneficial for photocatalytic reaction. Fig. S2 is the EDS elemental mapping of PCN. It can be observed that C, N and P elements evenly distributed, and the P-doping content was determined to be 0.13% (atomic percentage, shown in Table S1), revealing that P element was successfully doped into g-C_3N_4. In addition, Fig. 2c is the HRTEM image of PCN, as observed, the d-spacing of 0.34 nm can be well consistent with the (002) plane of g-C_3N_4. Fig. 2d is the TEM image of PCN/MoP, it can be discerned that many granular substances are embedding on PCN nanosheets. From the HRTEM images of Fig. 2e-f, the nanoparticle grown on the surface of PCN presents the lattice fringe with d-spacings of 0.32 and 0.21 nm, corresponding to the (001) and (101) plane of MoP in hexagonal phase, respectively [34]. What's more, it can
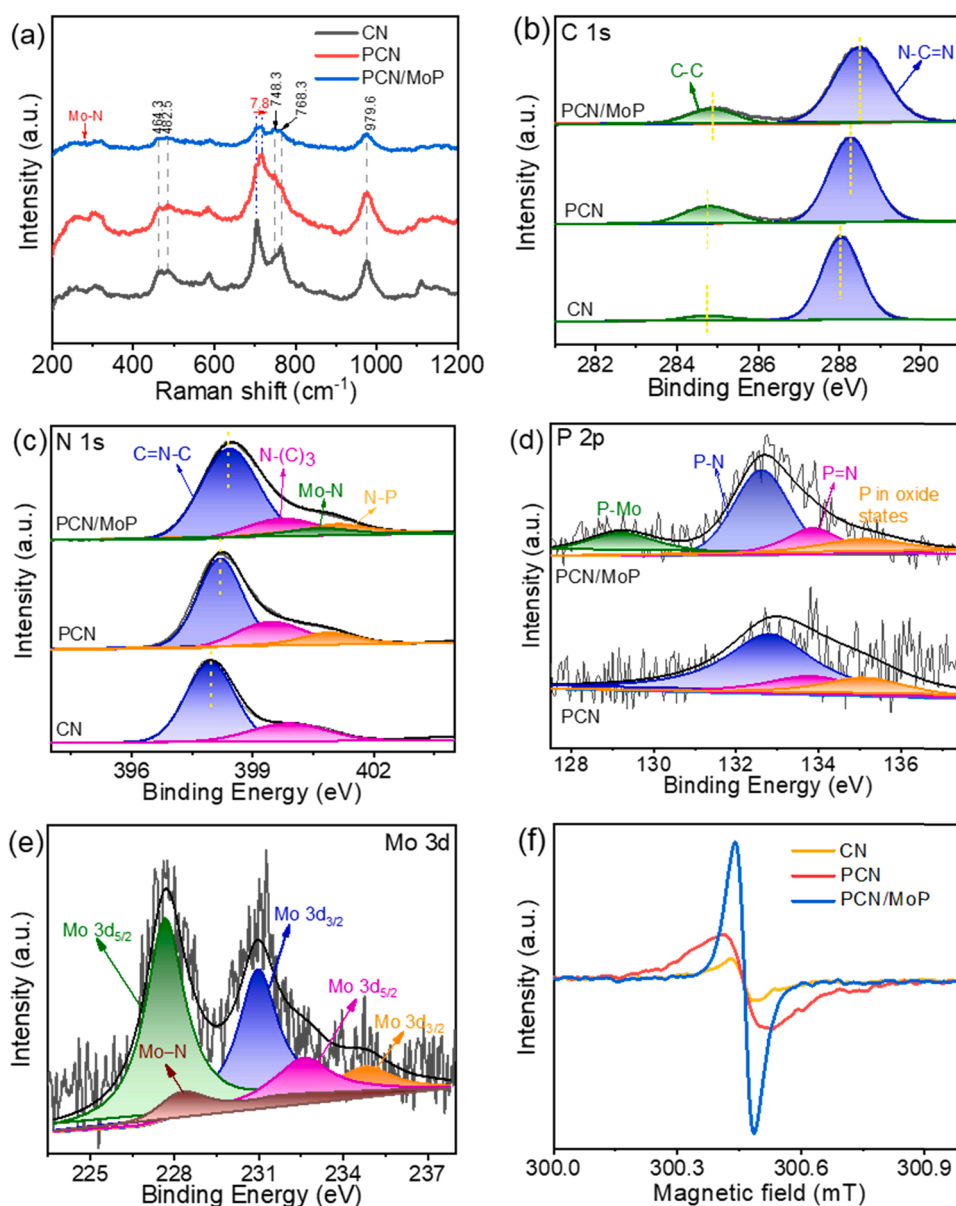

Fig. 3. (a) Raman spectrum of CN, PCN and PCN/MoP. (b) C 1s and (c) N 1s over CN, PCN and PCN/MoP. (d) P 2p over PCN and PCN/MoP. (e) Mo 3d over PCN/MoP. (f) EPR spectra of CN, PCN and PCN/MoP.

be noted that the lattice fringe of PCN and MoP contact closely, illustrating the intimate interfacial connection was formed between PCN and MoP, which is beneficial for the transfer and separation of photocarriers. Fig. 2g-k are the EDS element mapping of PCN/MoP, it can be noticed that the C and N elements distributing uniformly followed the PCN nanosheets, while the Mo and P elements distribute intensively over the granular region on the surface of PCN nanosheet. The above results further confirm the successful synthesize of PCN/MoP heterojunction photocatalyst.

Raman spectrum was further applied to investigate the molecular structure information of the synthesized photocatalyst (the result is showing in Fig. 3a). As observed in the Raman spectra of CN, the characteristic peaks located at 464.3 and 482.5 cm^{-1} can be assigned to the in-plane twisting vibration of heptazine heterocycle, the peaks at 748.3 and 768.3 cm^{-1} belong to the out-of-plane bending mode of graphitic domains in g-C$_3$N$_4$, the peak at 705.1 cm^{-1} corresponds to the breathing modes of s-triazine rings, and the peak at 979.6 cm^{-1} are contributed from the bending vibration of =C(sp^2) [35–37]. Besides, PCN shows the similar characteristic peak with CN, but the peak corresponding to s-triazine rings (712.9 cm^{-1}) presents slightly positive shift of 7.8 cm^{-1} in comparison to that in CN, suggesting that P atom was doped in CN and changed the chemical environment of s-triazine rings in CN. Moreover, PCN/MoP appears the basically consistent Raman peak with PCN except that the peak intensity in PCN/MoP show apparently decrease, which may be ascribed to combined action of abundant structural defects generated in PCN during the secondary ball-milling process and the deposition of MoP on the surface of PCN. In addition, it should be noted that an additional peak located at about 279.6 cm^{-1} can be distinguished in the Raman spectra of PCN/MoP, which can be corresponded to the signal of Mo-N [38], demonstrating that MoP nanoparticles were combined with PCN through forming Mo—N bond. Additionally, as shown in the Fourier-transform infrared (FTIR) spectra shown in Fig. S5, a peak at around 650 cm^{-1} was observed in PCN/MoP, which can be corresponded to the out-of-plane stretching vibrations mode of Mo—N bond [39], further confirming the formation of Mo—N between PCN and MoP under high-energy ball-milling effect. X-ray photoelectron spectroscopy (XPS) was further conducted to gain insights into the surface chemical states. Fig. S3 is the XPS survey spectrum of CN, PCN and PCN/MoP. As observed, only C, N and O elements can be discerned in the XPS spectrum of pristine CN, while P element can be observed in PCN, suggesting that P element exists in PCN photocatalyst. Furthermore, in addition to C, N and O elements, Mo and P elements can also be observed in the XPS survey spectrum of PCN/MoP, and the peak intensity of P 2p in PCN/MoP is stronger than that in PCN, revealing that MoP nanoparticles were attached on the surface of PCN. Furtherly, as observed in Fig. 3b, the C 1 s of the pristine CN shows two distinct peaks at 284.6 and 288.3 eV, corresponding to the sp^3-hybridized graphite C—C species and N—C=N species, respectively [40]. In comparison, the C 1s spectra in PCN presents distinctly shift to the higher energy region, which indicates that P atom with more free-electron was doped into CN, resulting in the increased electron cloud density over PCN. Furtherly, it can be clearly observed that the XPS peaks in C 1s spectra of PCN/MoP exhibit a further positive shift compared to PCN, suggesting the strong interfacial interaction between MoP and PCN induced by secondary high-energy ball-milling process. As shown in Fig. 3c, the N 1s of CN can be deconvoluted into two peaks, where the peaks located at 398.5 eV can be assigned to C—N=C from sp^2-hybridized nitrogen in triazine rings, and the peak at 400.2 eV belongs to the N-(C)$_3$ from tertiary nitrogen [40]. For the N 1s of PCN, a new peak located at 401.4 eV was discovered, which can be well corresponded to the N—P bond, verifying that a part of P atom was doped into g-C$_3$N$_4$ through replacing C atom and bonding with N atom [41]. For PCN/MoP photocatalyst, in addition to the peaks corresponding to C—N=C, N-(C)$_3$ and N—P bond, a new peak centered at 401 eV can be discerned, which can be assigned to the Mo—N bond, demonstrating that high-energy ball-milling procedure could bring about the interfacial chemical bond connection, which

would strongly contribute to the charge transfer and separation dynamics in PCN/MoP heterojunction photocatalyst. In addition, it can also be discovered that the CN=C and N-(C)$_3$ peaks in N 1s spectrum of PCN perform obvious shift to the high energy region than that in CN, further indicating the increased electron cloud density over PCN than CN due to the integration of P atom into g-C$_3$N$_4$ [42]. The positive shift of N 1s in PCN/MoP than that in PCN should be caused by the Mo—N bond forming. As observed in the P 2p spectrum showing in Fig. 3d, three main peaks can be found in PCN, where the peaks located at 132.8 and 133.8 eV can be assigned to P–N and P=N bond respectively, further demonstrating that P atom was doped into g-C$_3$N$_4$ by replacing a part of C atom, and the peak at 135.1 eV was corresponded to the P atom in high oxide states [14]. As for the PCN/MoP sample, in addition to the peaks of P–N, P=N and P–O bonds, a new peak sited at 129.2 eV can be discerned, which can be well corresponded to the Mo-P bond in MoP, confirming that MoP was indeed deposited on the surface of PCN through Mo—N bond [43]. Fig. 3e is the Mo 3d spectrum of PCN/MoP, in which, the peaks at 227.77 and 231.1 eV can be assigned to the Mo3d$_{5/2}$ and 3d$_{3/2}$ in MoP, respectively, which is consistent with the previous reports [23]. Meanwhile, the peaks at 231.57 and 234.77 eV can be indexed to the Mo3d$_{5/2}$ and 3d$_{3/2}$ in MoO$_x$, respectively, which should be ascribed to the slightly oxidization of MoP [44]. In addition to the above peaks, a peak at 228.2 eV can also be distinguished in Mo 3d spectra, which can be indexed to Mo—N bond in PCN/MoP [45], further verifying that MoP was deposited on the surface of PCN through forming interfacial Mo—N bond. To further investigate the existence of Mo—N bond, the XPS spectra of Mo 3d spectra in MoP was also carried out, and compared with the Mo 3d spectra in PCN/MoP. As observed in Fig. S4, the binding energy of Mo 3d in PCN/MoP exhibits slight negative-shift compared to that in MoP, demonstrating the strong chemical interaction between MoP and PCN. The shift of binding energy should be ascribed to that the electronegativity of N (3.1) is larger than that of P (2.1), thus the bonding effect between Mo and N would lead to the decreased electron cloud density around Mo atom in PCN/MoP than that in MoP. The above results confirm that high-energy ball-milling process can not only introduce P atom into g-C$_3$N$_4$, but also can establish intense interfacial chemical bond combination between MoP and PCN, which would strongly contribute to the charge transfer process. Fig. 3f is the electron paramagnetic resonance (EPR) spectra of CN, PCN and PCN/MoP. As shown, all the tested samples present one independent Lorentz derived line at g-value= 2.00012 originated from the unpaired electronic signals of sp^2-hybridized carbon atoms in the conjugated aromatic ring. It can be noted that the PCN exhibits an enhanced EPR signals than that of pristine CN, reflecting the better electron delocalization ability in PCN, which should be attributed to that P doping contributes to more solitary electron pairs in PCN [46,47]. Moreover, the EPR resonance of PCN/MoP is further improved than that of PCN, demonstrating the higher free electron density in PCN/MoP than that of PCN, which should be attribute to the following two aspects. Firstly, the secondary ball-milling process for preparing PCN/MoP heterostructure photocatalyst generated abundant structural defects in PCN/MoP, which can trap number of free electrons. Secondly, due to the different work function between PCN and MoP, the electron in PCN would transfer to MoP to equilibrate the Fermi level, which would give rise to the increase of free electrons in PCN/MoP than that in PCN. The electron drift has also been confirmed in the following DFT calculation results. As the charge redistribution, Schottky barrier would be formed at the surface of PCN/MoP and would accelerate the photocarriers separation.

3.3. Photocatalytic H$_2$ evolution activity

To reveal the synergetic promotion effect of P doping and MoP decorating on the photocatalytic H$_2$ production activity of PCN/MoP thoroughly, the H$_2$ evolution performance of the as-prepared various photocatalysts were compared and presented in Fig. 4. As observed in Fig. 4a, within two hours of irradiation, the CN/0.05MoP photocatalyst
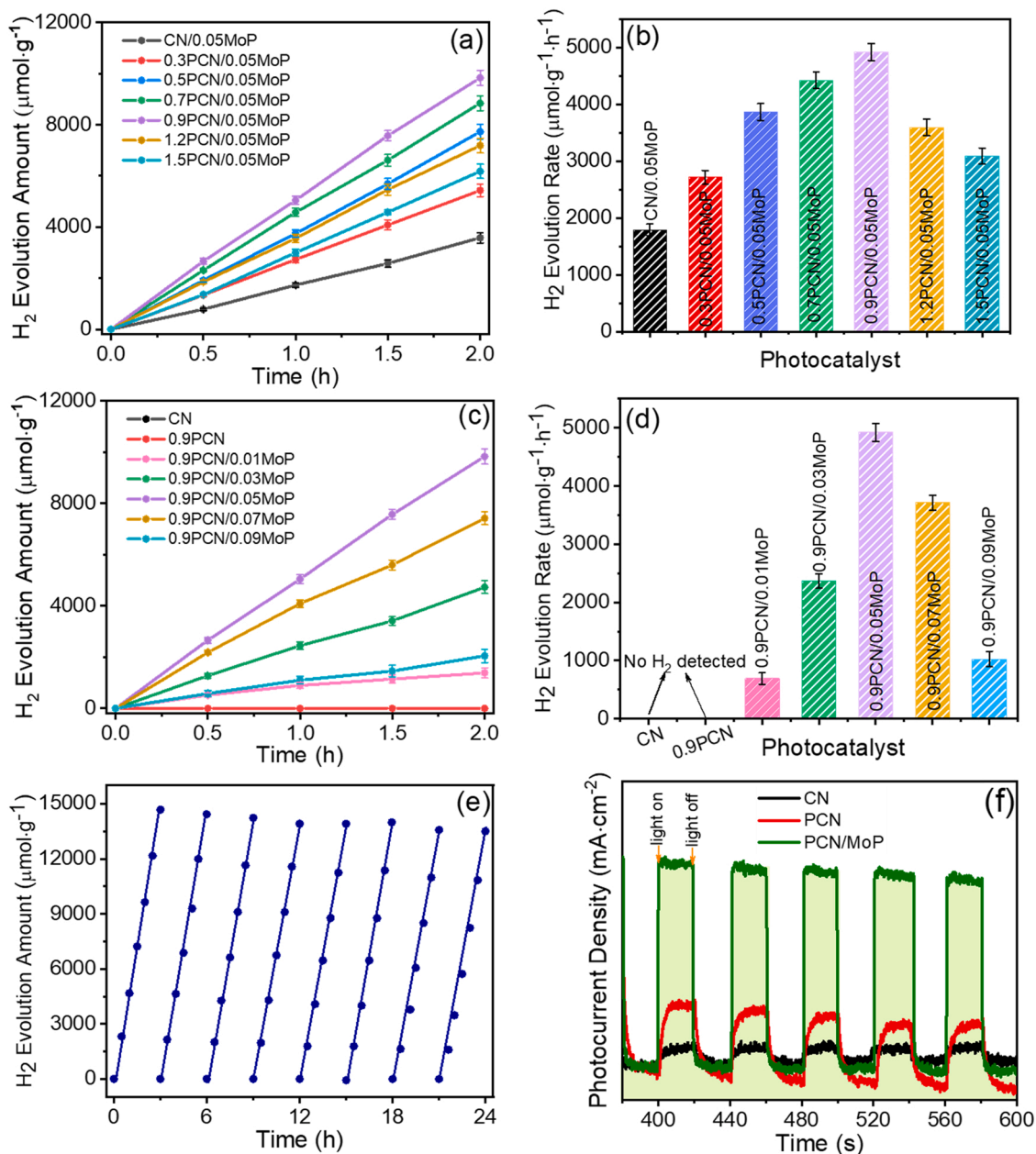
Fig. 4. (a) H_2 evolution amount at different irradiation time and (b) H_2 evolution rate over CN/0.05MoP and PCN/0.05MoP with different mass ratio of NaH_2-PO_2·$2H_2O$ to CN. (c) H_2 evolution amount at different irradiation time and (d) H_2 evolution rate over CN, 0.9PCN and PCN/MoP with different mass ratio of MoP to 0.9PCN. (e) Photocatalytic H_2 evolution stability test of PCN/MoP. (f) Photocurrent test of CN, PCN and PCN/MoP.

performs only 3579.92 µmol g^{-1} of H_2 production (H_2 evolution rate of 1789.96 µmol g^{-1} h^{-1}), but PCN/0.05MoP present evidently higher H_2 evolution amount and rate. It can be noted that when the mass ratio of NaH_2PO_2·H_2O to CN was adjusted to 0.9:1, the 0.9PCN/0.05MoP shows the most excellent photocatalytic activity with a H_2 production of 9835.65 µmol·g^{-1} in 2 h (H_2 evolution rate of 4917.83 µmol·g^{-1}·h^{-1}), indicating that the optimized P-doping content with the mass ratio of 0.9:1 for NaH_2PO_2·$2H_2O$ to CN can be obtained. The photocatalytic activity influenced by P-doping content could be attributed to that the moderate P atom doping could introduce the suitable mid-gap states in the band gap of g-C_3N_4, which can not only broaden the light absorbance range, but also promote the transfer of photogenerated electrons. Fig. 4c-d display the photocatalytic H_2 evolution activity of CN, 0.9PCN and 0.9PCN/MoP with different mass ratio of MoP to 0.9PCN. As shown, the pristine CN and 0.9PCN present no H_2 production, while 0.9PCN/MoP perform obviously improved H_2 evolution amount, demonstrating

that MoP-decorating contributes to the photocatalytic activity of g-C_3N_4. It can be discerned that the H_2 evolution amount of 0.9PCN/MoP increases with the mass ratio of MoP to 0.9PCN increasing. When the mass ratio of MoP to 0.9PCN was 0.05:1, the 0.9PCN/0.05MoP exhibits the highest H_2 evolution amount (9835.65 µmol g^{-1}) in 2 h with a H_2 evolution rate of 4917.83 µmol g^{-1} h^{-1} (as shown in Fig. 4b). With the mass ratio of MoP to 0.9PCN further increases, the H_2 evolution rate decreases, which should be ascribed that the excess MoP not only could cover the active sites of PCN, but also led to the too dark color of PCN/MoP for bringing about the shielding effect in the photocatalytic reaction liquid [48]. The H_2 evolution activity of PCN/MoP exceeds most of the g-C_3N_4-based photocatalysts reported recently, even some Pt-cocatalyst involving photocatalytic system (Table. S2 in Supporting Information). More importantly, the preparation of PCN/MoP is the simple, rapid, solvent-free and large-scale high-energy ball-milling technology, which endows the PCN/MoP with the more remarkable

practical application prospect.

In addition to H$_2$ evolution efficiency, the photocatalytic cycling stability is another important factor deciding the practical application of photocatalyst. As shown in Fig. 4e, during eight consecutive photocatalytic tests in 24 h, the 0.9PCN/0.05MoP photocatalyst performs the basically consistent H$_2$ evolution amount. Through the XRD, TEM and XPS characterizations (Fig. S7 and S8 in the Supporting Information), the 0.9PCN/0.05MoP after photocatalytic test exhibits the basically consistent morphology, phase structure and chemical composition with that before photocatalytic test, revealing the favorable structural and composition stability of the synthesized PCN/MoP photocatalyst, which should be attributed to the strong combination action between PCN and MoP by forming Mo—N bond during high-energy ball-milling process. Fig. 4f shows the transient photocurrent response spectrum of CN, PCN and PCN/MoP photocatalyst under 300 W Xe lamp. Obviously, the PCN/MoP exhibits the more significant photocurrent density than that of CN and PCN, revealing the more efficient photocarriers separation and transfer efficiency of PCN/MoP photocatalyst, which is consistent with the above photocatalytic H$_2$ evolution results. The relationship between the H$_2$ evolution apparent quantum efficiency (AQE) at different incident light wavelength (380, 420, 500 and 600 nm) and UV–vis absorbance spectra of the optimized PCN/MoP photocatalyst is presented in

Fig. S6 in Supporting Information. As observed, the AQE values at 380, 420, 500 and 600 nm are calculated to be 36.8%, 4.6%, 0.92%, 0.003%, respectively, matches well with the UV–vis absorbance of PCN/MoP, signifying the favorable light to H$_2$ transfer efficiency in the synthesized PCN/MoP photocatalyst.

3.4. Photocatalytic mechanism analysis

Density functional theory (DFT) calculation was carried out to investigate the role of P atom in PCN. Fig. 5a-b show the calculated band structure of CN and PCN, respectively. It can be noted that the band gap of PCN is 1.05 eV, narrower than that of CN (1.23 eV), reflecting that the PCN can be excited by incident light with longer wavelength and lower energy [49]. Furthely, as observed in the density of states (DOS) images (Fig. 5c-d), the valence band maximum (VBM) of CN was dominated by the contribution of N, while the conduction band minimum (CBM) was mainly contributed by C and N, which is consistent with the reported results [50]. As for the PCN, the VBM are mainly contributed by N species, whereas the CBM are predominantly contributed by C, N and a small fraction of P. Additionally, PCN presents a significantly increased DOS compared to CN, illustrating that the introduction of P atom can affect the electron properties of CN to a great extent, and thus resulting
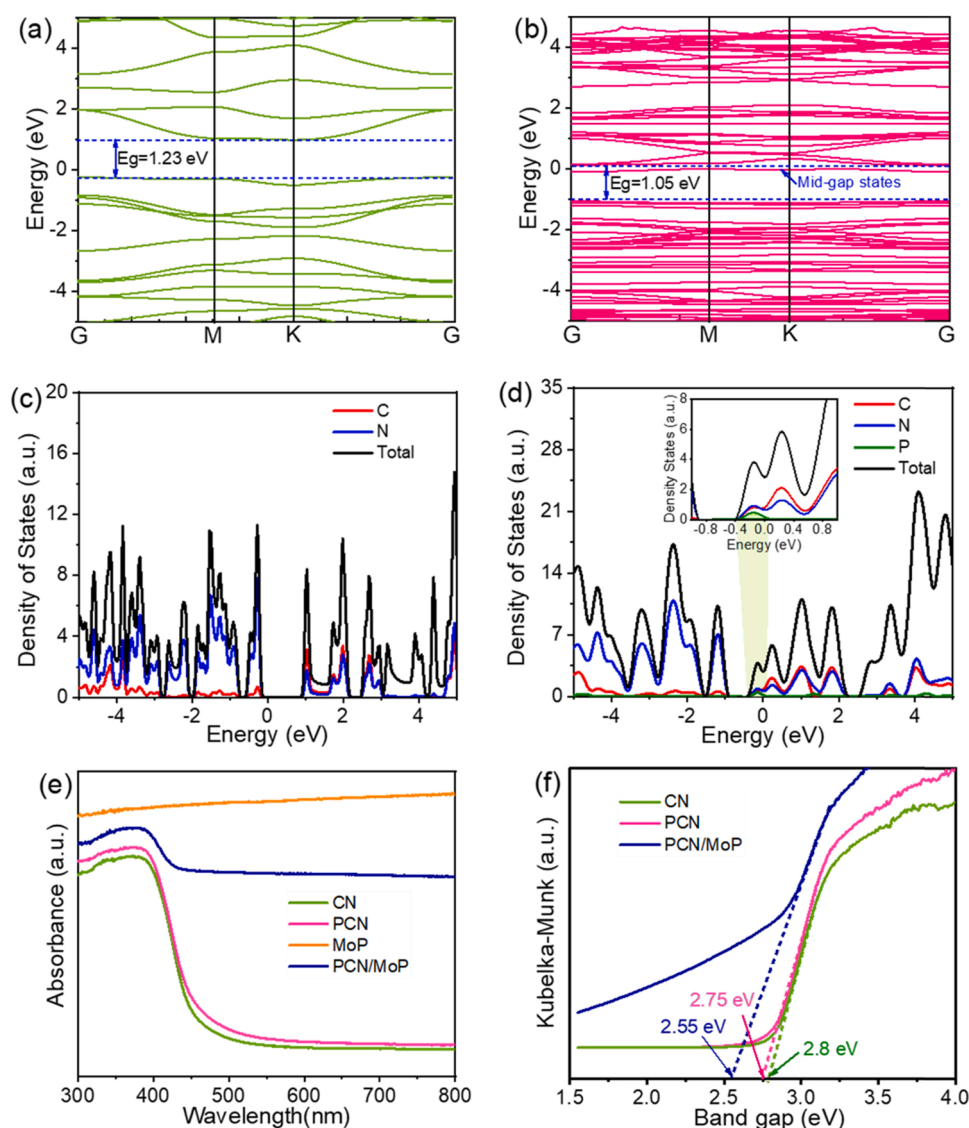

Fig. 5. Band structure of (a) CN and (b) PCN. Density of states (DOS) of (c) CN and (d) PCN. (e) UV–vis absorbance spectrum and (f) the transferred Kubelka-Munk vs the energy of incident light plots of CN, PCN, MoP and PCN/MoP.

in the higher charge carriers concentration, which could finally contribute to the enhanced photocatalytic activity of PCN/MoP than that of CN/MoP [51]. Interestingly, it can be noted that an empty mid-gap state arising from the hybridization of C, N and P species appear below the CBM of PCN, which can trap the electrons from the VB of PCN photoexcited by longer wavelength, thus greatly contributes to the light absorbance and photogenerated electrons transfer capacity [15]. Fig. 5e is the UV–vis absorbance spectrum of CN, PCN, MoP and PCN/MoP. It can be discerned that MoP shows a plat plot with a high adsorption coefficient throughout the UV–vis wavelength range, indicating that MoP exhibits a metallic character [23]. Meanwhile, P doping in g-C$_3$N$_4$ contributes to the slightly red-shift in the absorbance spectrum as compared with the original CN, corresponding to the narrower band gap of PCN, besides, it can be observed that the light absorbance intensity of PCN is higher than that of CN in the whole 300–800 nm wavelength region, suggesting that P doping can significantly influence the light absorbance capacity of CN. Clearly, the light absorbance intensity and wavelength range of PCN/MoP is further extended than that of PCN, which should be ascribed to the narrower band gap and the intense light absorbance capacity of MoP. Fig. 5f is the Kubelka-Munk vs. the energy of incident light plots, where the band gap value of CN, PCN and PCN/MoP can be determined to be 2.8, 2.75 and 2.55 eV, respectively. The narrower band gap is beneficial for the generation of photogenerated charge carriers, and thus benefiting for the photocatalytic activity.

In order to investigate the effect of P doping on the band structure of g-C$_3$N$_4$, and illustrate the photocatalytic mechanisms of PCN/MoP, the ultraviolet photoelectron spectroscopy (UPS) was conducted to investigate the energy levels of CN, PCN and MoP. According to the UPS spectra shown in Fig. 6a, the work function (W$_F$) of CN, PCN and MoP can be determined to be 4.32, 4.4 and 4.75 eV, respectively, by subtracting the secondary cutoff binding energy (E$_{cutoff}$, determined by extrapolating the linear part to the base line of the UPS spectra) from the excitation energy (21.22 eV) [52]. The 0.08 eV reduction of W$_F$ illustrates the increased electrons density in PCN than CN, which is in favor of the generation of photogenerated charge carriers. Mott-Schottky measure was conducted out to obtain the more detailed information of the band structure. As shown in Fig. 6b-c, the flat band potential (E$_{fb}$) of CN and PCN can be obtained to be − 1.15 and − 1.03 eV vs. NHE, respectively, by extending the liner part of Mott-Schottky plots to C^{-2} = 0 at the frequencies of 100 Hz, 200 Hz and 300 Hz. Besides that, it can be observed that the slope on Mott-Schottky plots of CN and PCN are positive, suggesting that they are n-type semiconductor. As for n-type semiconductor, the conduction band (CB) edge potential is approximately equal to the E$_{fb}$ [53], therefore, the CB edge potential (E$_{CB}$) of CN and PCN can be approximately determined to be − 1.15 and − 1.03 eV vs. NHE, respectively. According to the result of UV–vis absorbance spectra, the band gap (E$_g$) of CN and PCN were determined as 2.8 and 2.75 eV, respectively. Based on the relation of E$_{VB}$ = E$_g$ + E$_{CB}$, the valence band potential (E$_{VB}$) of CN and PCN can be intended to 1.65 and 1.72 eV vs. NHE, respectively. The above results further confirm that the P doping could affect the band structure of g-C$_3$N$_4$. Based on the above analysis, the relative band structure of CN, PCN and MoP can be depicted in Fig. 6d. It can be discerned that the E$_f$ of PCN (E$_{f:PCN}$) is higher than that of MoP (E$_{f:MoP}$), which signifies that the free electron in PCN would transfer to MoP until forming an equilibrium state of E$_f$
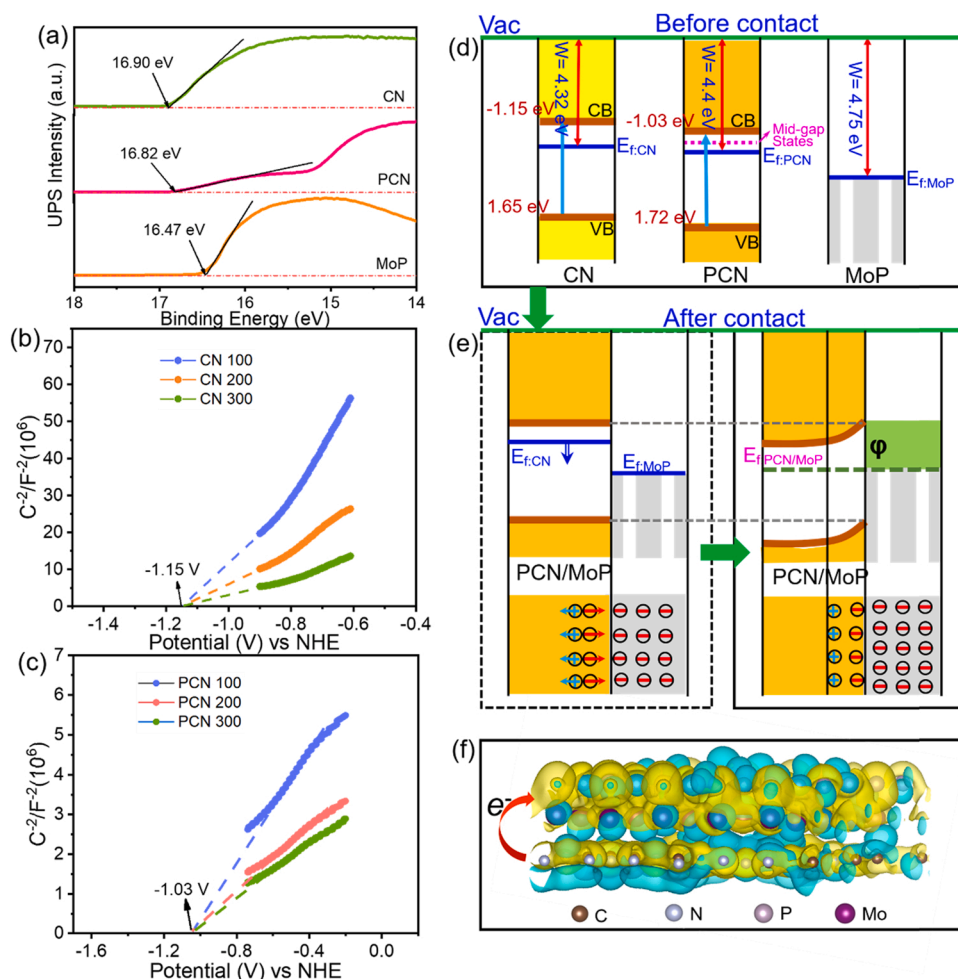

Fig. 6. (a) Ultraviolet photoelectron spectroscopy (UPS) of CN, PCN and MoP. Mott-Schottky (M-S) plot of (b) CN and (c) PCN at different frequency (100, 200 and 300 Hz). (d) Band alignment of CN, PCN and MoP. (e) The diagram of charge transfer in PCN/MoP heterostructure before the light illuminates. (f) Charge density difference of PCN/MoP heterostructure, where the yellow and cyan regions represent the charge accumulation and depletion. (For interpretation of the references to colour in this figure, the reader is referred to the web version of this article.)

between $E_{f:PCN}$ and $E_{f:MoP}$. In detail, as depicted in Fig. 6e, when PCN contacted with MoP intimately, the free electrons in PCN near the PCN/MoP interface would diffuse to MoP with lower E_f level. The electrons drifting would lead to that MoP side are enriched with negative electrons, and the depletion layer would be formed in PCN side near the PCN/MoP interface, which would therefore lead to the down-shift of $E_{f:PCN}$. With the ongoing drift of electrons, the $E_{f:PCN}$ would fall to the level near $E_{f:MoP}$, and the CB and VB of PCN bend downward, leading to the formation of Schottky barrier (as shown in the right section of Fig. 6e). The electrons drifting between PCN and MoP can also be intuitively observed in the charge density difference map showing in Fig. 6f. It can be discovered that the MoP is mainly occupied by yellow color, whereas the PCN is primarily covered by cyan color, suggesting that the electrons in PCN migrate to MoP, further verifying the above speculate about charge transfer process. The Gibbs free-energy of HER for PCN/MoP was calculated by a three-state diagram consisting of initial state $H^+ + e^-$, intermediate adsorbed H* and the final product $1/2 H_2$. As shown in Fig. S11, PCN/MoP exhibits a positive and near to zero Gibbs free-energy of 0.129 eV over the intermediate state (ΔG_{H*}), implying the weak hydrogen adsorption kinetic, which is beneficial for the enhancement of photocatalytic H_2 evolution performance.

Furthermly, due to that the PCN near MoP are negative charged (contains more electrons), while the side away from the MoP are positive charged (contains more holes), an internal electric field would be formed in the depletion layer of PCN. When the PCN/MoP photocatalyst was illuminate by light, the photoinduced holes in the VB of PCN would transfer to the side near the PCN/MoP interface, remaining more photogenerated electrons in the CB of PCN. When PCN/MoP photocatalyst was continuously illuminated by light, as illustrated in Fig. 7a, the

photoexcited carriers would be generated largely, resulting abundant photogenerated electrons accumulated in the CB of PCN. These accumulated electrons would possess enough energy to overcome the Schottky barrier and transfer to the surface of MoP to participate in water splitting reaction. It is worth mentioning that the Schottky barrier between MoP and PCN can impede the electrons on the surface of MoP reflux to PCN, while the photoinduced holes would be left in PCN and react with TEOA. Moreover, the interfacial Mo—N bond serving as the "delivery channels" could effectively speed up the transfer of photogenerated electrons from PCN to MoP, further improves the separation and migration of photoexcited carriers. Besides that, the mid-gap state under the CB of PCN can serve as the trapping center of the electrons excited by incident light with longer wavelength, and therefore broaden the light absorbance and promote the photogenerated electrons transfer. Under the synergistic effect of P-doping, Mo—N bond and Schottky barrier, the photogenerated electrons in PCN can be irreversibly delivered to MoP, which participate in water splitting reaction fleetly, therefore realizing efficient photocatalytic H_2 evolution activity of PCN/MoP photocatalyst.

To further reveal the positive effect of the P-doping, Mo—N bonding and Schottky barrier on photocatalytic mechanism, and give the direct evidence for the improved H_2 evolution performance of PCN/MoP photocatalyst, electrochemical impedance spectra (EIS), steady-state PL spectra and time-resolved transient PL decay spectra (TRPL) were carried out. As observed in Fig. S4, the pristine CN photocatalyst presents the largest Nyquist plots arc radius, demonstrates the poor charge mobility. In comparison, the arc radius of PCN appears apparently decreased, intuitively reflects that the introduction of P atom can reduce the charge transfer resistance in CN. Moreover, it can be noted that the
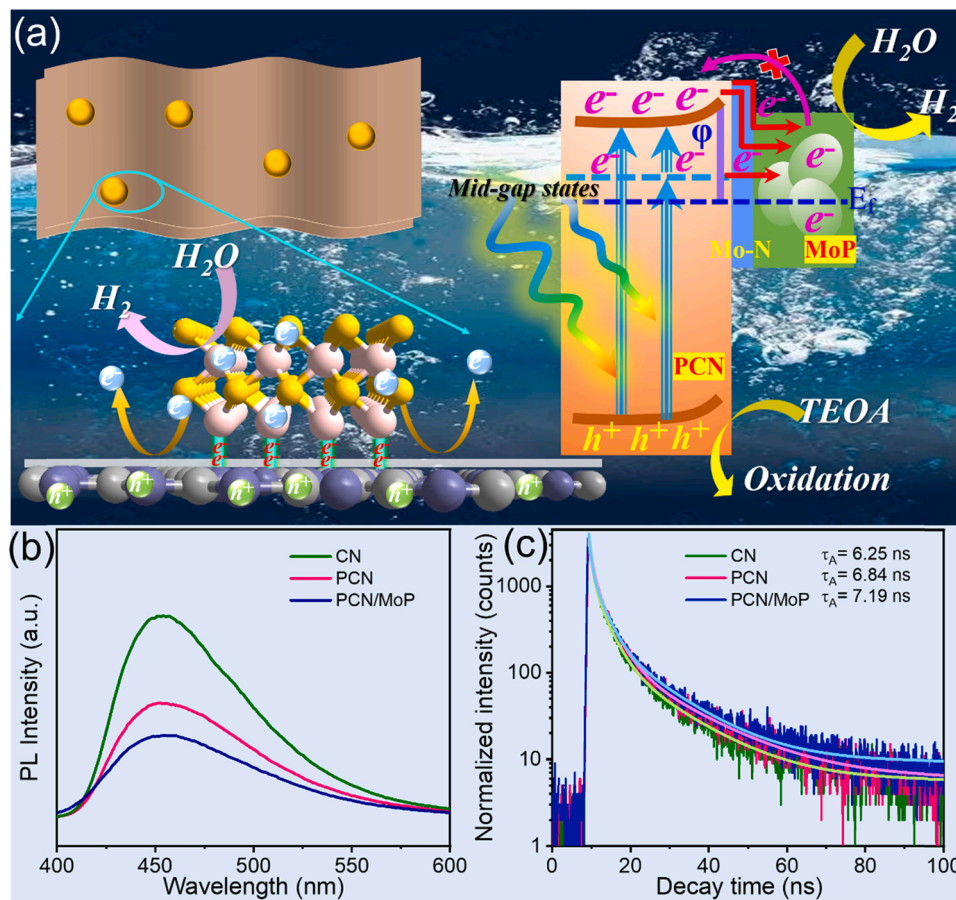

Fig. 7. (a, b) Diagram of photocatalytic H_2 production process and mechanism over PCN/MoP heterojunction. (c) Steady-state PL emission spectra and (d) time-resolved transient PL decay (TRPL) spectra of CN, PCN and MoP.

PCN/MoP displays the further decreased arc radius, suggests the significantly improved electrical conductivity of PCN by combining with MoP, which is beneficial for the transfer and separation of photocarriers, and finally contributes to the photocatalytic activity. Fig. 7b shows the PL spectra of CN, PCN and PCN/MoP, as shown, CN presents the most significant emission peak intensity, suggesting the serious recombination of electron-hole pairs. In comparison, the PCN photocatalyst exhibits an obvious decreased PL peak intensity, implying that P atom doping can effectively motivate the separation of photocarriers, which should be attributed to the generation of electronic capture center on the surface of CN with the introduction of P atom. It is worth noting that the PCN/MoP heterostructure displays the lowest PL peak intensity, signifies the significantly promoted photocarriers separation by integrating PCN with MoP through Mo—N bond, and establishing the Schottky barrier. TRPL is a useful means to reveal the charge carriers lifetime and photocatalytic reaction dynamics. Fig. 7c displays the TRPL spectra of CN, PCN and PCN/MoP, which was fitted by the following triple-exponential fitting equation (Eq. 1) to obtain the quantitative information of photocarriers lifetime:

$$Fit = A + B_1 exp\left(-\frac{t}{\tau_1}\right) + B_2 exp\left(-\frac{t}{\tau_2}\right) + B_3 exp\left(-\frac{t}{\tau_3}\right) \qquad (1)$$

The specific fitting results was shown in Table S3 in the Supporting Information. The average emission lifetime (τ_A) could be calculated by the following tri-exponential fitting method (Eq. 2):

$$\tau_A = \frac{A_1\tau_1^2 + A_2\tau_2^2 + A_3\tau_3^2}{A_1\tau_1 + A_2\tau_2 + A_3\tau_3} \qquad (2)$$

Accordingly, the PL emission lifetime of CN was determined to be 6.25 ns, while the PCN presents a PL emission lifetime of 6.84 ns. The longer PL lifetime suggests the inhibited photocarriers recombination in PCN. In an obvious contrast, PCN/MoP photocatalyst presents the longest PL emission lifetime of 7.19 ns, signifies the further accelerated photocarriers transfer and separation rate by combining with MoP, which contributed to the improved photocatalytic H$_2$ evolution activity of PCN/MoP.

To sum up, the improved photocatalytic H$_2$ production property of PCN/MoP was realized by P atom doping, interfacial Mo-N "delivery channels" establishing, and PCN/MoP Schottky barrier constructing, which gave rise to the increased light harvesting capacity, the narrowed band gap, the decreased charge transfer resistance, especially the inhibited recombination and the promoted separation of photocarriers.

4. Conclusions

In conclusion, through a simple, efficient, solvent-free and large-scale high-energy ball-milling procedure, P-doping and MoP-decorating g-C$_3$N$_4$ (PCN/MoP) photocatalyst was synthesized. The optimal 0.9PCN/0.05MoP photocatalyst performs the high photocatalytic H$_2$ evolution rate of 4917.83 μmol·g^{-1}·h^{-1} without any noble-metal cocatalyst, and favorable recycling stability by keeping almost constant H$_2$ evolution rate during five continuous cycles. Mechanism study reveal that the favorable H$_2$ production activity of PCN/MoP profit from the synergistical effect of P-doping, Mo-N chemical bonding and Schottky barrier. In detail, P-doping contributes to the enhanced light absorbance capacity and electrical conductivity by influencing the band structure of g-C$_3$N$_4$, Schottky barrier inside PCN/MoP promoted the photocarriers separation by inhibiting the photogenerated electrons refluxing from MoP to PCN, more importantly, the interfacial Mo—N bond accelerated the transfer and separation of photogenerated charge carriers by serving as effective electrons "delivery channels" between PCN and MoP. This present study not only prepares an efficient noble-metal-free photocatalyst for H$_2$ production, but also establishes a constructive reference for assembling other effective photocatalyst through high-energy ball-milling procedure on a large scale.

CRediT authorship contribution statement

Xuehua Wang: Methodology, Investigation, Data curation, Formal analysis, Writing – original draft . **Xianghu Wang**: Methodology, Investigation, Data curation, Formal analysis. **Wenli Tian**: Methodology, Investigation, Data curation, Formal analysis. **Xuehua Wang**: Writing – original draft. **Alan Meng**: Writing – review & editing, Formal analysis. **Zhenjiang Li**: Writing – review & editing, Investigation, Funding acquisition. **Shaoxiang Li**: Conceptualization, Methodology, Supervision, Funding acquisition. **Lei Wang:** Conceptualization, Methodology, Supervision, Funding acquisition. **Guicun Li**: Conceptualization, Methodology, Supervision, Funding acquisition.

Declaration of Competing Interest

The authors declare that they have no known competing financial interests or personal relationships that could have appeared to influence the work reported in this paper.

Acknowledgement

Appendix A. Supporting information

Supplementary data associated with this article can be found in the online version at doi:10.1016/j.apcatb.2021.120933.

References

[1] P. Zhang, L.J. Wu, W.G. Pan, S.C. Bai, R.T. Guo, Efficient photocatalytic H$_2$ evolution over NiS-PCN Z-scheme composites via dual charge transfer pathways, Appl. Catal. B Environ. 289 (2021), 120040.

[2] K. Julia, J.S. Alberto, S. Gökcen, R. Petra, M. Igor, K. Kathrin, S. Hendrik, A.V. G. Hugo, D. Viola, G. Lars, B.D. Cem, S. Metin, P. Filip, O. Christian, V.L. Bettina, Photocatalytic hydrogen evolution: interfacial engineering for improved photocatalysis in a charge storing 2D carbon nitride: melamine functionalized poly (heptazine imide, Adv. Energy Mater. 11 (2021) 2003016.

[3] F. Chen, T.Y. Ma, T.R. Zhang, Y.H. Zhang, H.W. Huang, Atomic-level charge separation strategies in semiconductor-based photocatalysts, Adv. Mater. 33 (2021) 2005256.

[4] Y.P. Zhu, T.Z. Ren, Z.Y. Yuan, Mesoporous phosphorus-doped g-C$_3$N$_4$ nanostructured flowers with superior photocatalytic hydrogen evolution performance, ACS Appl. Mater. Interfaces 7 (30) (2015) 16850–16856.

[5] Z.K. Shen, M. Cheng, Y.J. Yuan, L. Pei, J.S. Zhong, J. Guan, X.Y. Li, Z.J. Li, L. Bao, X.F. Zhang, Z.T. Yu, Z.G. Zou, Identifying the role of interface chemical bonds in activating charge transfer for enhanced photocatalytic nitrogen fixation of Ni$_2$P-black phosphorus photocatalysts, Appl. Catal. B Environ. 295 (2021), 120274.

[6] J.Q. Di, M. Zhang, Y.X. Chen, J.X. Wang, S.S. Geng, J.Q. Tang, Z.H. Zhang, Copper anchored on phosphorus g-C$_3$N$_4$ as a highly efficient photocatalyst for the synthesis of N-arylpyridin-2-amines, Green. Chem. 23 (2021) 1041–1049.

[7] A. Seongjoon, K. Gwangwoo, K.N. Pramoda, Y. Seong In, L. Hyunseob, S. Hyun-Joon, S. Hyeon Suk, Prevention of transition metal dichalcogenide photodegradation by encapsulation with h-BN layers, ACS Nano 10 (9) (2016) 8973–8979.

[8] A.L. Meng, W.L. Tian, H. Yang, X.H. Wang, X.H. Wang, Z.J. Li, Molybdenum sulfide-modified metal-free graphitic carbon nitride/black phosphorus photocatalyst synthesized via high-energy ball-milling for efficient hydrogen evolution and hexavalent chromium reduction, J. Hazard. Mater. 413 (2021), 125400.

[9] P. Sulagna, S. Dipti Prava, P. Kulamani, Recent advances in anion doped g-C$_3$N$_4$ photocatalysts: a review, Carbon 172 (2020) 682–711.

[10] X. Zhang, X.Z. Yuan, L.B. Jiang, J. Zhang, H.B. Yu, H. Wang, G.M. Zeng, Powerful combination of 2D g-C$_3$N$_4$ and 2D nanomaterials for photocatalysis: recent advances, Chem. Eng. J. 390 (2020), 124475.

[11] J.L. Shi, T. Yuan, M.F. Zheng, X.C. Wang, Metal-free heterogeneous semiconductor for visible-light photocatalytic decarboxylation of carboxylic acids, ACS Catal. 11 (5) (2021) 3040–3047.

[12] X.Q. Wei, X. Wang, Y. Pu, A.N. Liu, C. Chen, W.X. Zou, Y.L. Zheng, J.S. Huang, Y. Zhang, Y.C. Yang, M. Naushad, B. Gao, L. Dong, Facile ball-milling synthesis of CeO$_2$/g-C$_3$N$_4$ Z-scheme heterojunction for synergistic adsorption and photodegradation of methylene blue: characteristics, kinetics, models, and mechanisms, Chem. Eng. J. 420 (2020), 127719.

[13] S. Liu, H.L. Zhu, W.Q. Yao, K. Chen, D.M. Chen, One step synthesis of P-doped g-C$_3$N$_4$ with the enhanced visible light photocatalytic activity, Appl. Surf. Sci. 430 (2018) 309–315.

[14] Y.J. Zhou, L.X. Zhang, J.J. Liu, X.Q. Fan, B.Z. Wang, M. Wang, W.C. Ren, J. Wang, M.L. Li, J.L. Shi, Brand new P-doped g-C$_3$N$_4$: enhanced photocatalytic activity for H$_2$ evolution and rhodamine B degradation under visible light, J. Mater. Chem. A 3 (2015) 3862–3867.

[15] J.R. Ran, T.Y. Ma, G.P. Gao, X.W. Du, S.Z. Qiao, Porous P-doped graphitic carbon nitride nanosheets for synergistically enhanced visible-light photocatalytic H$_2$ production, Energy Environ. Sci. 8 (2015) 3708–3717.

[16] H.Y. Yang, Y.M. Zhou, Y.Y. Wang, S.C. Hu, B.B. Wang, Q. Liao, H.F. Li, Jh Bao, G.Y. Ge, S.K. Jia, Three-dimensional flower-like phosphorus-doped g-C$_3$N$_4$ with a high surface area for visible-light photocatalytic hydrogen evolution, J. Mater. Chem. A 6 (2018) 16485–16494.

[17] S. Bai, J. Jiang, Q. Zhang, Y.J. Xiong, Steering charge kinetics in photocatalysis: intersection of materials syntheses, characterization techniques and theoretical simulations, Chem. Soc. Rev. 44 (2015) 2893–2939.

[18] X.J. She, H. Xu, Y.H. Yu, L.L. Li, X.W. Zhu, Z. Mo, Y.H. Song, J.J. Wu, S.Q. Yuan, H.M. Li, Accelerating photogenerated charge kinetics via the synergetic utilization of 2D semiconducting structural advantages and noble-metal-free schottky junction effect, Small 15 (2019) 1804613.

[19] X.J. Wang, X. Tian, Y.J. Sun, J.Y. Zhu, F.T. Li, H.Y. Mu, J. Zhao, Enhanced schottky effect of a ^{2}D–^{2}D CoP/g-C$_3$N$_4$ interface for boosting photocatalytic H$_2$ evolution, Nanoscale 10 (2018) 12315–12321.

[20] X.H. Wang, X.H. Wang, J.F. Huang, S.X. Li, A.L. Meng, Z.J. Li, Interfacial chemical bond and internal electric field modulated Z-scheme S$_v$-ZnIn$_2$S$_4$/MoSe$_2$ photocatalyst for efficient hydrogen evolution, Nat. Commun. 12 (2021) 4112.

[21] W.P. Xiao, L. Zhang, D. Bukhvalov, Z.P. Chen, Z.Y. Zou, L. Shang, X.F. Yang, D.Q. Yan, F.Y. Han, T.R. Zhang, Hierarchical ultrathin carbon encapsulating transition metal doped MoP electrocatalysts for efficient and ph-universal hydrogen evolution reaction, Nano Energy 70 (2019), 104445.

[22] Y. Song, N.J. Li, D.Y. Chen, Q.F. Xu, H. Li, J.H. He, J.M. Lu, 3D ordered MoP inverse opals deposited with CdS quantum dots for enhanced visible light photocatalytic activity, Appl. Catal. B Environ. 238 (2018) 255–262.

[23] Q.D. Yue, Y.Y. Wan, Z.J. Sun, X.J. Wu, Y.P. Yuan, P.W. Du, MoP is a novel, noble-metal-free cocatalyst for enhanced photocatalytic hydrogen production from water under visible light, J. Mater. Chem. A 3 (2015) 16941–16947.

[24] D. Jean-Louis, F. Tomislav, Mechanochemistry: a force of synthesis, ACS Cent. Sci. 3 (2017) 13–19.

[25] G. Kresse, J. Furthmüller, Efficiency of ab-initio total energy calculations for metals and semiconductors using a plane-wave basis set, Comput. Mater. Sci. 6 (1996) 15–50.

[26] T. Bučko, J. Hafner, S. Lebègue, J.G. Ángyán, Improved description of the structure of molecular and layered crystals: ab initio DFT calculations with van der Waals corrections, J. Phys. Chem. A 114 (2010) 11814–11824.

[27] B. Hammer, L.B. Hansen, J. Rskov, Improved adsorption energetics within density-functional theory using revised Perdew-Burke-Ernzerhof functionals, Phys. Rev. B 59 (1999) 7413–7421.

[28] J.P. Perdew, K. Burke, M. Ernzerhof, Generalized gradient approximation made simple, Phys. Rev. Lett. 77 (1998) 3865–3868.

[29] G. Kresse, D. Joubert, From ultrasoft pseudopotentials to the projector augmented-wave method, Phys. Rev. B 59 (1999) 1758–1775.

[30] P. Blöchl, O. Jepsen, O.K. Andersen, Improved tetrahedron method for Brillouin-zone integrations, Phys. Rev. B 49 (1994) 16223.

[31] S. Grimme, S. Ehrlich, L. Goerigk, Effect of the damping function in dispersion corrected density functional theory, J. Com. Chem. 32 (2011) 1456–1465.

[32] V. Wang, N. Xu, J.C. Liu, G. Tang, W.T. Geng, VASPKIT: a user-friendly interface facilitating high-throughput computing and analysis using VASP code, Comput. Phys. Commun. 267 (2019), 108033.

[33] S.D. Sun, X. Zhang, J. Cui, Q. Yang, S.H. Liang, High-index faceted metal oxide micro-/nanostructures: a review on their characterization, synthesis and applications, Nanoscale 11 (2019) 15739–15762.

[34] W. Zong, N.B. Chui, Z.H. Tian, Y.Y. Li, C. Yang, D.W. Rao, W. Wang, J.J. Huang, J.T. Wang, F.L. Lai, T.X. Liu, Ultrafine MoP nanoparticle splotched nitrogen-doped carbon nanosheets enabling high-performance 3D-printed potassium-ion hybrid capacitors, Adv. Sci. 8 (2021) 2004142.

[35] X.D. Zhang, J. Yan, F.Y. Zheng, J. Zhao, L.Y. Suk Lee, Designing charge transfer route at the interface between WP nanoparticle and g-C$_3$N$_4$ for highly enhanced photocatalytic CO$_2$ reduction reaction, Appl. Catal. B Environ. 286 (2021), 119879.

[36] J.X. Ni, D.M. Liu, W. Wang, A.W. Wang, J.L. Jia, J.Y. Tian, Z.P. Xing, Hierarchical defect-rich flower-like BiOBr/Ag nanoparticles/ultrathin g-C$_3$N$_4$ with transfer channels plasmonic Z-scheme heterojunction photocatalyst for accelerated visible-light-driven photothermal-photocatalytic oxytetracycline degradation, Chem. Eng. J. 419 (2021), 129969.

[37] X.D. Zhang, D. Kim, J. Yan, L.Y. Suk Lee, Photocatalytic CO$_2$ reduction enabled by interfacial S-scheme heterojunction between ultrasmall copper phosphosulfide and g-C$_3$N$_4$, ACS Appl. Mater. Interfaces 13 (2021) 9762–9770.

[38] J. Xiong, W.W. Cai, W.J. Shi, X.L. Zhang, J. Li, Z.H. Yang, L.G. Feng, H.S. Cheng, Salt-templated synthesis of defect-rich MoN nanosheets for boosted hydrogen evolution reaction, J. Mater. Chem. A 5 (2017) 24193–24198.

[39] G. Jaysiva, S. Manavalan, S.M. Chen, P. Veerakumar, M. Keerthi, H.S. Tu, MoN nanorod/sulfur-doped graphitic carbon nitride for electrochemical determination of chloramphenicol, ACS Sus. Chem. Eng. 8 (30) (2020) 11088–11098.

[40] K.H. Chen, X.W. Wang, Q.Y. Li, Y.N. Feng, F.F. Chen, Y. Yu, Spatial distribution of ZnIn$_2$S$_4$ nanosheets on g-C$_3$N$_4$ microtubes promotes photocatalytic CO$_2$ reduction, Chem. Eng. J. 418 (2021), 129476.

[41] L. Jing, R.X. Zhu, D.L. Phillips, J.C. Yu, Effective prevention of charge trapping in graphitic carbon nitride with nanosized red phosphorus modification for superior photo(electro)catalysis, Adv. Funct. Mater. 27 (2017) 1708484.

[42] P. Sulagna, S. Dipti Prava, P. Kulamani, Recent advances in anion doped g-C$_3$N$_4$ photocatalysts: a review, Carbon 172 (2021) 682–711.

[43] M. Guo, M.J. Xu, Y. Qu, C. Hu, P.X. Yan, T.T. Isimjan, X.L. Yang, Electronic/mass transport increased hollow porous Cu$_3$P/MoP nanospheres with strong electronic interaction for promoting oxygen reduction in Zn-air batteries, Appl. Catal. B Environ. 297 (2021), 120415.

[44] C. Cheng, S.C. Zong, J.W. Shi, F. Xue, Y.Z. Zhang, X.J. Guan, B.T. Zheng, J.K. Deng, L.J. Guo, Facile preparation of nanosized MoP as cocatalyst coupled with g-C$_3$N$_4$ by surface bonding state for enhanced photocatalytic hydrogen production, Appl. Catal. B Environ. 265 (2020), 118620.

[45] J. Ganesamurthi, M. Shaktivel, S.M. Chen, V. Pitchaimani, K. Murugan, H.S. Tu, MoN nanorod/sulfur-doped graphitic carbon nitride for electrochemical determination of chloramphenicol, ACS Sustain. Chem. Eng. 8 (2020) 11088–11098.

[46] Y.Y. Wang, Y.W. Zhang, S. Zhao, Z.W. Huang, W.X. Chen, Y.M. Zhou, X.S. Lv, S.H. Yuan, Bio-template synthesis of Mo-doped polymer carbon nitride for photocatalytic hydrogen evolution, Appl. Catal. B Environ. 248 (2019) 44–53.

[47] Y. Wang, W. Xu, Y. Zhang, Y.Z. Wu, Z.K. Wang, L. Fu, F.L. Bai, B.Y. Zhou, T.T. Wang, L. Cheng, J.Z. Shi, H. Liu, R. Yong, Introducing spin polarization into atomically thin 2D carbon nitride sheets for greatly extended visible-light photocatalytic water splitting, Nano Energy 83 (2021), 105783.

[48] Z.J. Li, X.H. Wang, W.L. Tian, A.L. Meng, L.N. Yang, CoNi bimetal cocatalyst modifying a hierarchical ZnIn$_2$S$_4$ nanosheet-based microsphere noble-metal-free photocatalyst for efficient visible-light-driven photocatalytic hydrogen production, ACS Sustain. Chem. Eng. 7 (2019) 20190–20201.

[49] P.F. Wang, Z.R. Shen, Y.G. Xia, H.T. Wang, L.R. Zheng, W. Xi, S.H. Zhan, Atomic insights for optimum and excess doping in photocatalysis: a case study of few-layer Cu-ZnIn$_2$S$_4$, Adv. Funct. Mater. 29 (2018) 1807013.

[50] J.D. Hu, C. Chen, T. Hu, J.S. Li, H. Lu, Y. Zheng, X.G. Yang, C.X. Guo, C.M. Li, Metal-free heterojunction of black phosphorus/oxygen-enriched porous g-C$_3$N$_4$ as an efficient photocatalyst for fenton-like cascade water purification, J. Mater. Chem. A 8 (2020) 19484–19492.

[51] X.D. Zhang, X. Xie, H. Wang, J.J. Zhang, B.C. Pan, Y. Xie, Enhanced photoresponsive ultrathin graphitic-phase C$_3$N$_4$ nanosheets for bioimaging, J. Am. Chem. Soc. 135 (2013) 18–21.

[52] J. Liu, Y. Liu, N.Y. Liu, Y.Z. Han, X. Zhang, H. Huang, Y. Lifshitz, S.T. Lee, J. Zhong, Z.H. Kang, Metal-free efficient photocatalyst for stable visible water splitting via a two-electron pathway, Science 347 (2015) 970–974.

[53] D.D. Zhu, Q.X. Zhou, Nitrogen doped g-C$_3$N$_4$ with the extremely narrow band gap for excellent photocatalytic activities under visible light, Appl. Catal. B Environ. 281 (2021), 119474.